e-Prime - Advances in Electrical Engineering, Electronics and Energy 12 (2025) 101034

Contents lists available at ScienceDirect

e-Prime - Advances in Electrical Engineering, Electronics and Energy

journal homepage: www.elsevier.com/locate/prime

Ultra-fast all-optical memory based on hexagonal photonic crystal lattice on a GaAs substrate

Dariush Jafari, Mohammad Danaie *

Faculty of Electrical and Computer Engineering, Semnan University, Semnan, Iran

ARTICLE INFO

Keywords:
Photonic crystals
Kerr effect
Optical memory
Optical hysteresis
Cavity
GaAs

ABSTRACT

In this paper, a novel photonic crystal (PhC) all-optical memory is proposed. It is based on a hexagonal lattice of air holes on a GaAs substrate. The structure is numerically simulated using the finite difference time domain (FDTD) method. This structure utilizes the nonlinear Kerr effect properties of a photonic crystal cavity to achieve high-speed performance with a rise time of <0.21 ps. The high Q factor of the hexagonal cavity, combined with the use of Kerr material, results in reduced power consumption for both the data and bias signals, reaching below 3 μW/μm. Additionally, the reduction in the dimensions of the structure to approximately 30 μm^2 is significant and noteworthy compared to recent works. Our innovative design highlights significant advancements in speed and power efficiency for the designed all-optical memory, suggesting promising applications in photonic integrated circuits.

1. Introduction

The rapid technology growth and the exponential increase in data volume have created an urgent need for advancements in the accuracy and speed of hardware components such as processors, transmission channels, and memory systems. Traditional electronic devices are fundamentally limited in achieving ultra-fast performance due to the inherent characteristics of electrons, which restricts their speed and efficiency when compared to photonic devices [1–3].

Photonic crystal (PhC) based devices have emerged as prime candidates for the development of high-speed components due to their ability to manipulate light with high precision and minimal energy loss. The integration of photonic crystals, particularly with nonlinear Kerr materials, can significantly enhance the functionality and performance of optical components. Nonlinear Kerr materials introduce intensity-dependent refractive indices, enabling dynamic control over light propagation and interaction within the photonic structures. This capability is essential for realizing high-speed, low-power optical devices, which are critical for the future of photonic integrated circuits (PIC) [4–6].

These devices leverage periodic dielectric structures to control the propagation of photons, resulting in enhanced performance characteristics. Among various photonic crystal devices, sensors [7–13], high-Q cavities [14–16], add-drop filters [17], power splitters [18–20], waveguide intersections [21–23], analog-to-digital converters [24], logic gates [25–28], switches [29,30], flip-flops [31], couplers [32,33] and memories [34] have shown remarkable potential.

All-optical memory is an essential component in the realization of all-optical processing circuits. Recent years have seen several papers reporting on all-optical memories using various methods. However, based on our knowledge, there have been relatively few efforts to realize all-optical memory cells utilizing photonic crystals [35–38].

By leveraging a nonlinear cavity and optical bistability, all-optical flip-flop operations can be effectively realized, serving as robust optical memory devices. However, one of the primary challenges in designing photonic integrated circuits (PICs) lies in the power consumption and physical dimensions of the memory cells. These memory structures are typically orders of magnitude larger than other circuit components, which adds complexity to the design process [39].

In this paper, we report on all-optical memory cells based on optical bistability utilizing a non-linear cavity composed of Kerr material in photonic crystal. The organization of this paper is as follows: Section 2 introduces the proposed structure. Section 3 is devoted to the calculations and analysis of the proposed structure. In Section 4, Tolerance Analysis in Fabrication, . In Section 5 simulation results will be discussed. Finally, Section 5 concludes the paper.

* Corresponding author.
E-mail address: danaie@semnan.ac.ir (M. Danaie).

https://doi.org/10.1016/j.prime.2025.101034
Received 29 December 2024; Received in revised form 22 April 2025; Accepted 25 May 2025
Available online 30 May 2025

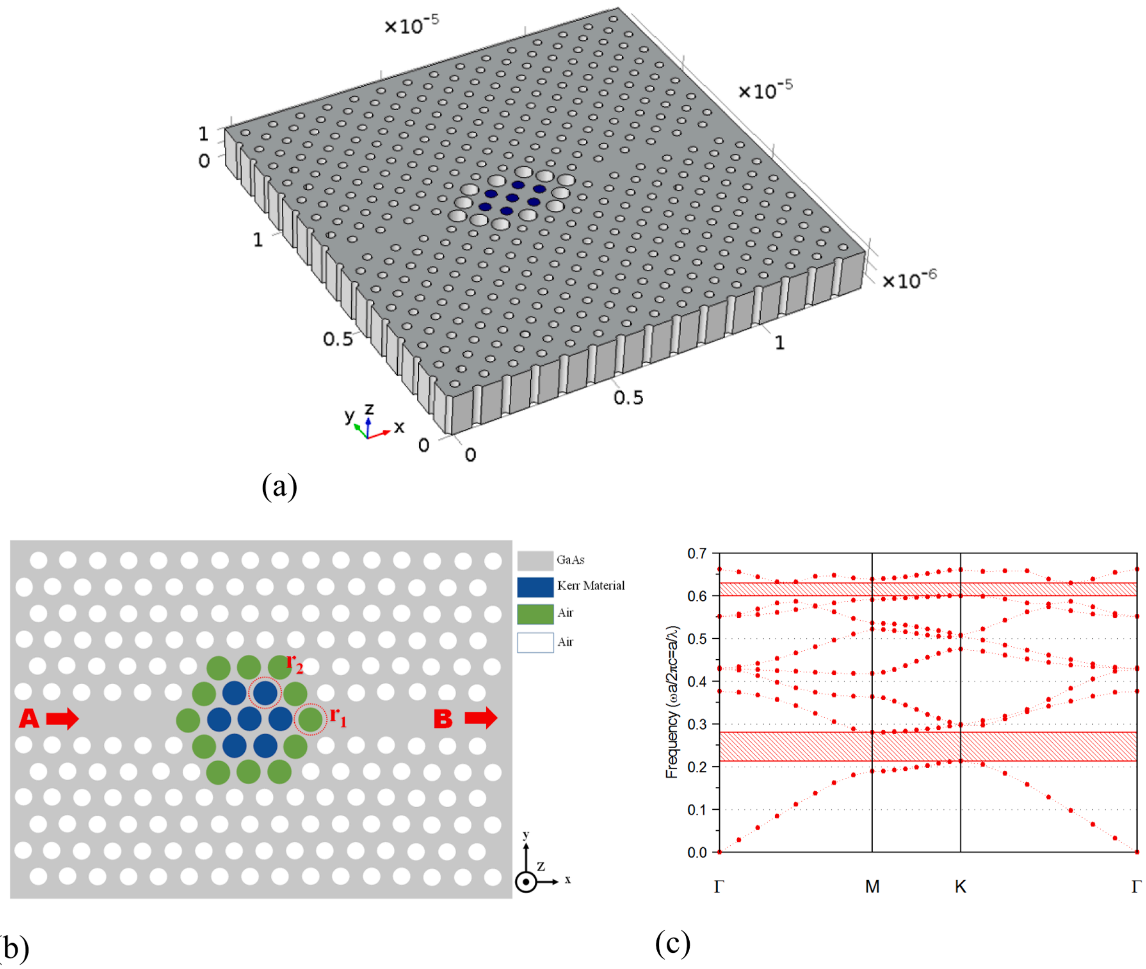

Fig. 1. (a and b) Proposed photonic crystal filter structure: 3D and 2D perspective views. (c) Photonic band diagram of the filter structure.

2. Design all-optical filter based photonic crystal cavity

In sophisticated photonic structures, such as logic gates, switches, and analog-to-digital (A/D) converters, the filtering mechanism plays a crucial role in device performance. Therefore, designing and simulating a PhC filter is a primary step. A filtering mechanism can be realized using a cavity coupled to a waveguide.

Fig. 1(a) demonstrates an optical filter structure, where Port A and Port B are considered the input and output ports, respectively. The cavity contains inner defects (green rods) and outer defects (blue rods). The substrate of the structure is GaAs, which has a refractive index of 3.49 at the wavelength of 1.555 µm, serving as the high refractive index material. The air holes, with a diameter of 0.3a, serve as the low refractive index material. The waveguide is created by removing one row of holes, with the lattice constant considered as $a = 405$ nm [39].

Bandgaps play a crucial role in defining the operational wavelengths and enhancing the performance of the photonic crystal filter. Fig. 1(b) illustrates the photonic band diagram of the proposed structure, which reveals two distinct band gaps. As shown in the figure, the wide band gap for the TE mode is observed in the normalized frequency range of 0.21–0.28 ($\omega a/2\pi c = a/\lambda$), which corresponds to a wavelength range from 1.928 µm to 1.448 µm. In contrast, the narrow band gap is located at a normalized frequency of 0.6, corresponding to a wavelength of 0.660 µm.

The resonant frequency of this cavity is primarily determined by the radius and refractive index of the defects. To systematically explore the influence of these parameters on the resonance wavelength of the cavity, a series of simulations were conducted. In each simulation, one parameter was varied while the others were held constant.

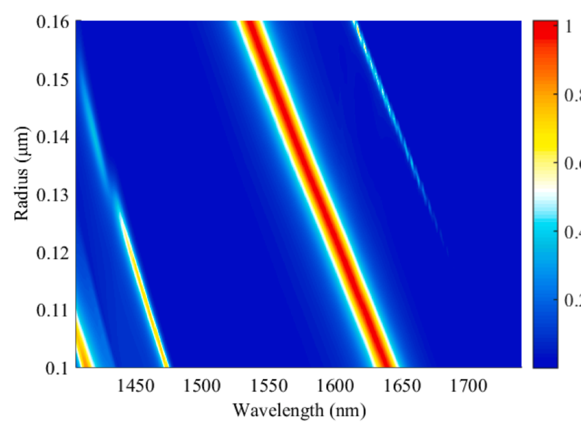

Fig. 2. Transmission spectrum of the resonator vs. inner defects r_1 as varied from 0.1a to 0.4a.

In the first step, the radius of the inner defects r_1 was varied from 0.1a to 0.4a, while the radius of the outer defects r_2 was fixed at 0.37a. The refractive index for r_1 was set to 2.6, and for r_2, it was set to 1. The transmission of the filter and the quality factor of the cavity were investigated using finite difference time domain (FDTD) simulations to obtain the filter transmission. The results of these simulation settings are shown in Fig. 2. As depicted, an increase in the outer defect radius causes a blue shift in the transmission spectrum. This shift indicates a

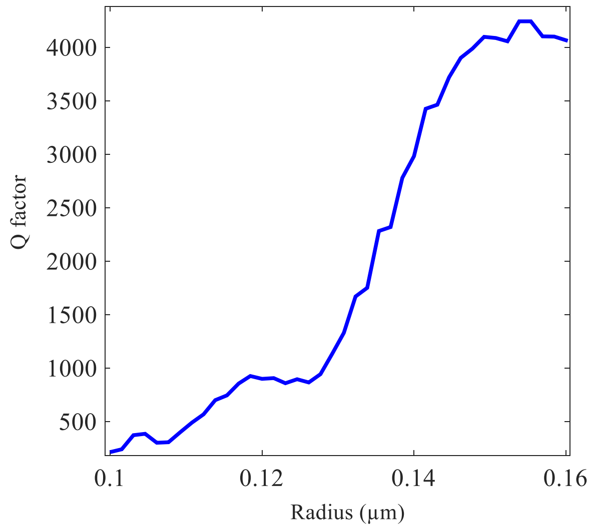

Fig. 3. The Q-factor of the cavity vs. inner defects r1 as varied from 0.1a to 0.4a.

movement towards shorter wavelengths in the transmission spectrum due to changes in the effective refractive index of the cavity, which affects the resonant frequency. By precisely controlling the defect sizes, we can fine-tune the operational wavelengths of the photonic crystal filter to achieve optimal performance for specific applications.

The Q-factor, plays a pivotal role in defining the performance of photonic crystal-based all-optical memory devices. It directly governs energy confinement, spectral selectivity, and photon lifetime within the resonator, influencing both data storage stability and response speed.

A high Q-factor signifies strong energy confinement and minimal optical losses, which enhances memory retention and resonance sharpness. In all-optical memory structures, this leads to prolonged photon lifetimes, ensuring that stored optical states maintain coherence over extended periods. However, this comes at the expense of switching speed, as the longer cavity lifetime inherently slows down the rate at which the system transitions between memory states.

Conversely, a lower Q-factor facilitates faster decay of stored photons, leading to rapid response times and improved dynamic switching. This is critical for high-speed photonic logic operations where memory updating and signal processing need to occur within femtosecond or picosecond timescales. However, excessive reduction in Q-factor can degrade storage fidelity, as weaker resonance limits the efficiency of state preservation.

Optimizing the Q-factor for photonic crystal memory structures requires balancing stability and speed. Consequently, we analyze the Q-factor of the proposed structure by extracting it from the slope of the decaying envelope in the time-domain signal obtained via FDTD simulation. In this approach, the Q-factor is computed using the following formula

$$Q = \frac{-\omega_R log_{10}(e)}{2m}$$

In this eqution $\omega_R = 2\pi f_r$ is the angular frequency, f_r resonant frequency, and m is the slope of the logarithmic decay envelope obtained from the FDTD simulation.

Fig. 3 demonstrates the Q-factor of the cavity as a function of the outer inner radius. The results show how variations in the outer defect radius impact the Q-factor across different wavelengths. As shown in the figure, by altering the outer defect radius, the Q-factor reaches up to 4000.

In the second step, the outer defect radius r_2 is varied from 0.1a to 0.4a μm, while fixing the radius of the inner defects r_1 at 0.37a . The refractive index for r_1 is set to 2.6, and for r_2, it is set to 1. The transmission of the cavity is investigated again using these settings.

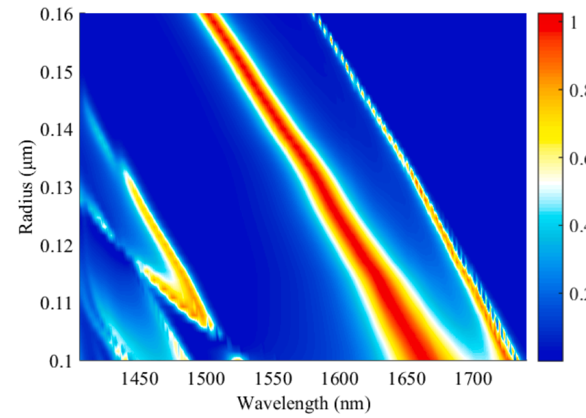

Fig. 4. Transmission spectrum of the resonator vs. outer defect radius r_2 as varied from 0.1a to 0.4a.

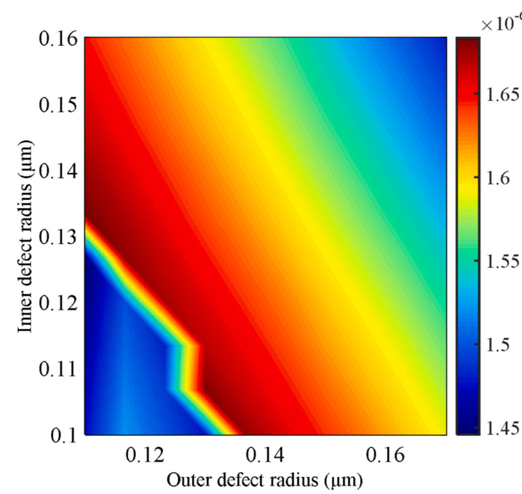

Fig. 5. Transmission spectrum of the transmission vs. outer defect radius r_2 as varied from 0.1a to 0.42a and inner defect radius r_1 as varied from 0.1a to 0.4a.

Fig. 4 shows the transmission spectrum of the structure. The behavior of the outer radius in the transmission spectrum is similar to that of the inner radius. It is clear that as the outer radius increases, a blue shift occurs in the transmission spectrum, indicating a move towards shorter wavelengths. This behavior highlights the significant impact of the outer defect radius on the operational characteristics of the photonic crystal filter.

To improve the optimization of the structure, a contour plot was introduced to provide a global view of the transmission behavior as a function of both inner and outer defect radii. In this representation, the X- and Y-axes correspond to r_1 and r_2, respectively, with the color bar indicating the wavelength of maximum transmission. The results of this analysis are presented in Fig. 5.

In this study, the outer defect radius was varied from 0.1a to 0.42a μm, while the inner defect radius was adjusted from 0.1a to 0.4a, keeping all other parameters constant. The resulting transmission intensity was recorded. As observed in the figure, the transmission intensity remains very low for radii below approximately 0.32a. However, for radii exceeding 0.32a μm, there is a sudden increase in transmission intensity, followed by a gradual decrease as the radii continue to increase. This trend highlights the significant influence of defect radii on the transmission characteristics of the photonic crystal filter, allowing for precise control of the transmission by tuning these parameters.

To ensure the accuracy of the simulation parameters and validate its

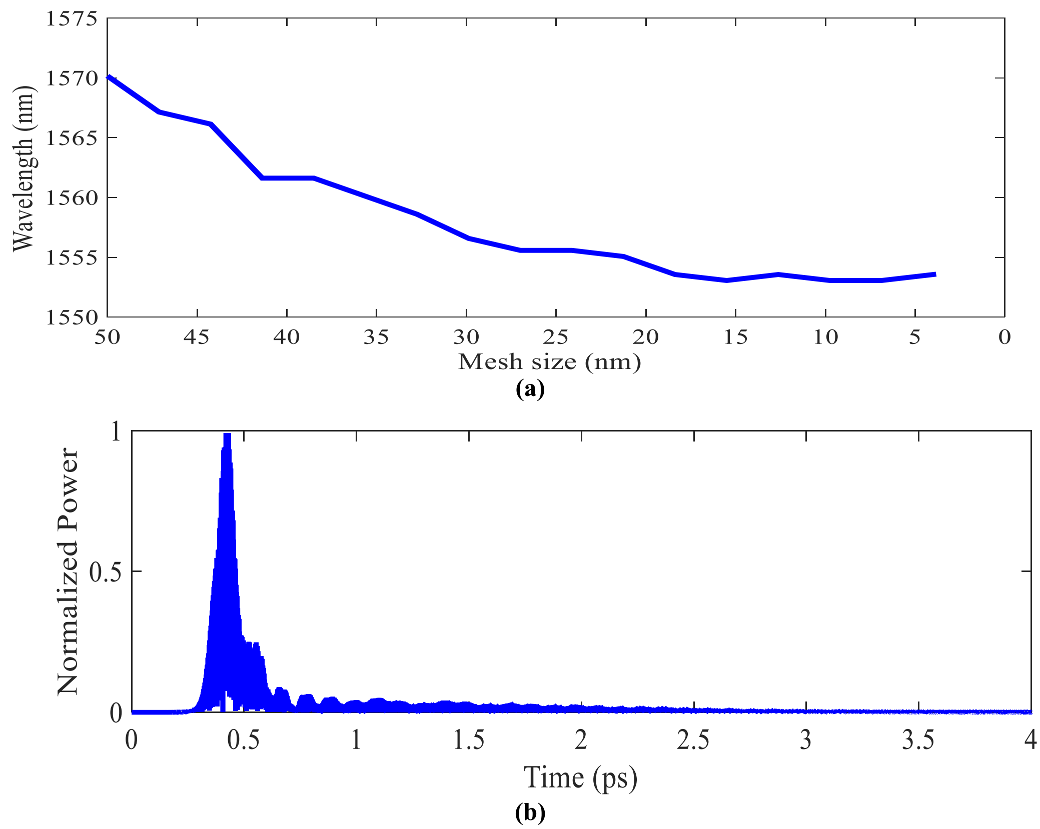

Fig. 6. (a) Effect of mesh resolution from 50 to 5 nm on the transmission wavelength. (b) Time-domain response for an input Gaussian pulse with a duration of 0.5 ps.

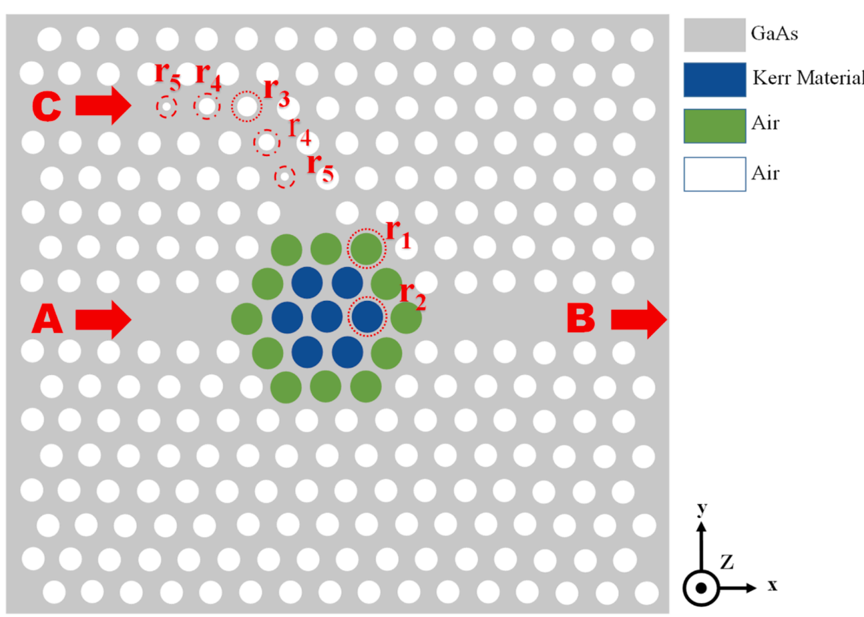

Fig. 7. proposed photonic crystal all-optical memory cell structure with the addition of Port C and five defects with radii r3, r4, and r5.

convergence, the following analyses were conducted. Fig. 6(a) illustrates the effect of mesh resolution on the transmitted wavelength. The mesh size was varied from 50 nm down to 5 nm, and the corresponding transmission wavelength was recorded. As shown in the figure, As the mesh resolution decreases from 50 nm to 20 nm, the transmission wavelength undergoes a shift from 1570 nm to 1555 nm. However, when the mesh size is further decreased below 20 nm, down to 5 nm, the transmission wavelength stabilizes and remains around 1555 nm. This result indicates that a mesh resolution of 20 nm or finer ensures convergence in the wavelength of maximum transmission.

Fig. 6(b) presents the time-domain response of the simulated structure. In this case, a Gaussian pulse with a duration of 0.5 ps and a spectral range spanning 400–1800 nm was introduced into the structure. The temporal output was recorded up to 4 ps. As shown in the figure, the transmitted signal decays completely by 3 ps, demonstrating that the simulation has achieved convergence.

Table 1
Simulation setting and structure parameters.

Parames	value	Description
a	0.405 (μm)	Lattice constant
Grid size	0.02 (μm)	Discretization resolution in simulations
Boudray conditions	PML	Perfectly matched layers used for absorption
PML layer width	0.5 (μm)	Thickness of the absorbing boundary region
N	3.4	Refractive index of the GaAs substrate Material [39,40]
n_0	2.6	Linear refractive index of the Inner defect Kerr defects [41]
n_2	2.7e-9 (m^2/w^2)	Nonlinear refractive index of the Inner defect Kerr InAs QD Material [41] defects
r_2	0.387a	Radius of the Inner defect
r_1	0.407a	Outer defect radius
r_3	0.25a	Radius of the waveguid defect
r_4	0.21a	Radius of the waveguid defect
r_5	0.07a	Radius of the waveguid defect

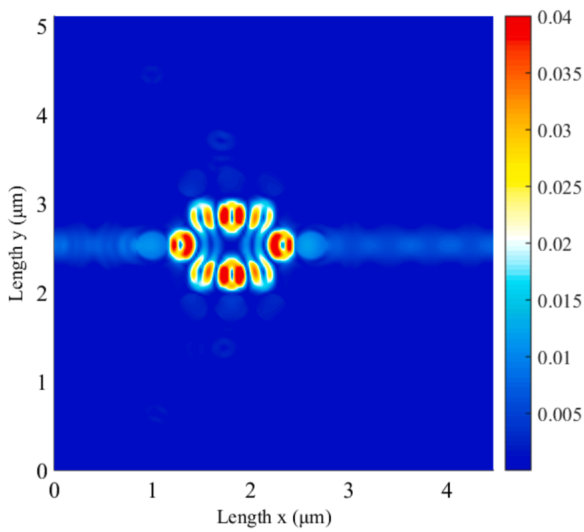

Fig. 8. Poynting vector (P) distributions of the proposed cavity structure.

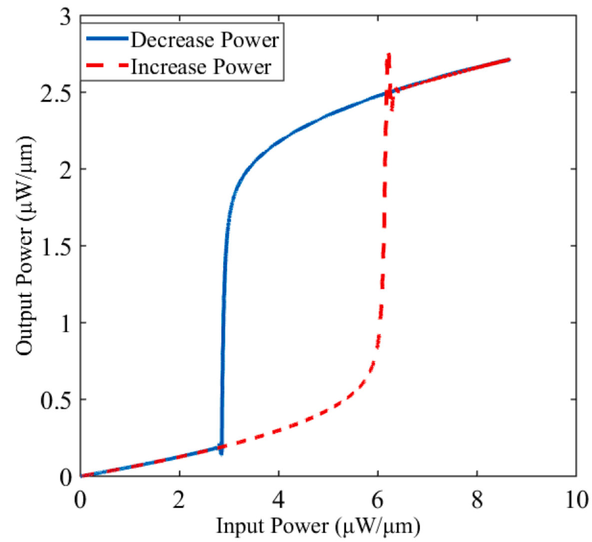

Fig. 10. Optical bistable hysteresis loop of the structure during the increase and decrease of the applied optical power.

3. Design of all-optical memory cell

The proposed all-optical memory cell is demonstrated in Fig. 7. The key difference between this structure and the filter structure is the addition of Port C. Ports A and B are considered as the input and output ports, respectively. To add Port C to the structure, five defects with radii r_3, r_4, and r_5 were incorporated. The addition of these defects is intended to facilitate the transmission of light with minimal losses at the operational wavelength of the structure. The parameters for the proposed memory cell are detailed in Table 1.

By incorporating Kerr nonlinear material in the inner defects, the refractive index increases with the increase in light intensity. This nonlinear property is crucial for the operation of the memory cell, enabling it to switch states based on the intensity of the incoming light.

Fig. 8 demonstrates the mode profile of the cavity. It is evident that light is well-confined within the cavity, resulting in a high light confinement factor. Consequently, as the light intensity inside the cavity increases, the refractive index also increases due to the Kerr nonlinear effect. This property is essential for the efficient operation of the memory cell, as it allows for the modulation of the refractive index based on

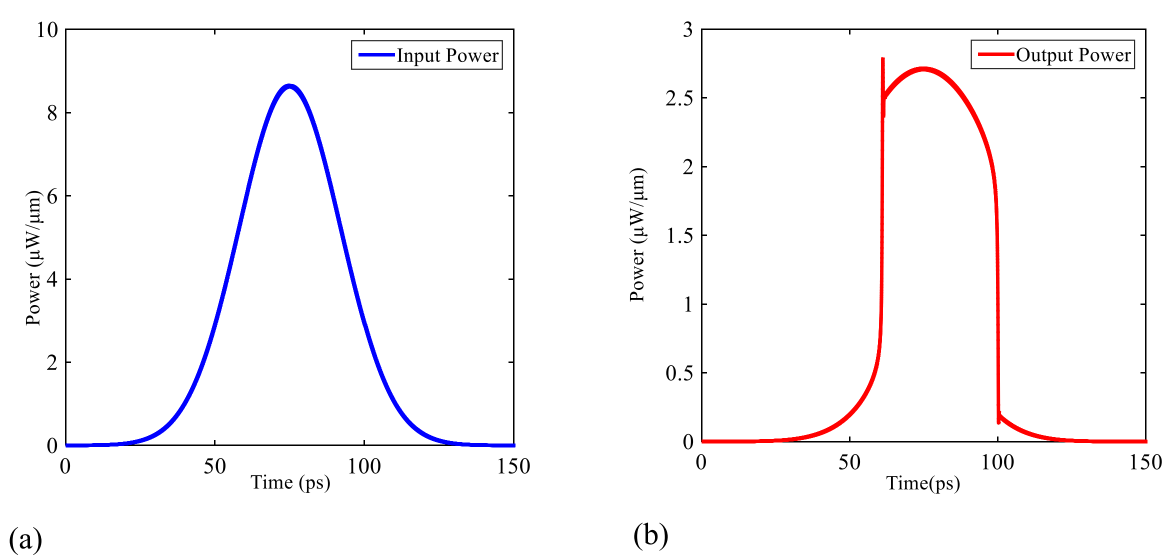

Fig. 9. Time domain simulation of the structure: (a) Gaussian pulse with duration 150 ps launched to Port A. (b) Time domain signal obtained from Port B.

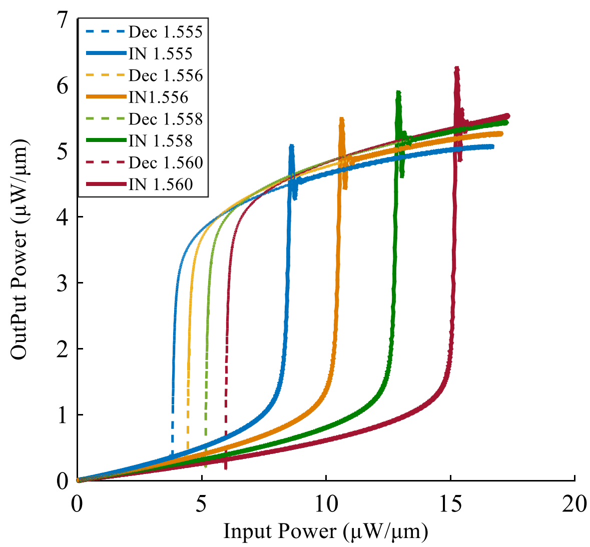

Fig. 11. Effects of wavelengths 1.555, 1.556, 1.557, and 1.560 μm on the bistability loop width of the proposed memory structure.

the intensity of the light, enabling effective light control and manipulation within the photonic structure.

4. Results and discussions

Fig. 9a shows a Gaussian pulse with a duration of 150 ps launched into Port A, leading to the observation of optical bistability at the output port, as depicted in Fig. 8b Initially, there is no signal at the output. When the input power reaches 6 μW/μm at 60 ps, the output signal suddenly appears, completing the first half of the bistability loop. The output follows the input signal until the input light intensity decreases to 2 μW/μm at 100 ps, at which point the output signal intensity drops to zero, completing the second half of the bistability loop.

The optical bistable hysteresis loop of the structure can be obtained from the time-varying output power versus input power, as shown in Fig. 10. In the first half of the loop, the output signal power remains in the low state when the input signal power is between 3 and 6 μW/μm. In the second half of the loop, an increase in the input signal power beyond 6 μW/μm causes the output to jump to the high state. This behavior demonstrates the hysteresis effect, where the output state depends not only on the current input power but also on the history of the input signal.

Next, four Gaussian pulses with wavelengths of 1.555, 1.556, 1.557, and 1.558 μm are applied to Port A. The detuning between these pulses and the cavity resonance wavelength modifies the bistable hysteresis loop profile of the memory cell. The results of this investigation are illustrated in Fig. 11. The diagram reveals that increasing the detuning between the input pulses and the cavity resonance wavelength enlarges the loop area, thereby enhancing the performance of the memory cell. This increase in loop area indicates improved stability and reliability in the memory cell's operation, highlighting the importance of precise wavelength control in optimizing device performance.

By applying a trigger signal from Port C of the structure, the output state can be effectively manipulated, functioning similarly to a memory cell. When the input signal power is maintained between 2 and 6 μW/μm, the operating point of the memory cell is positioned on the optical bistable hysteresis loop. For example, if the device is initially in a low state, the application of a trigger signal to Port C transitions the device to a high state. This behavior is illustrated in Fig. 12a and b, demonstrating the capability to control the memory cell's state through the trigger signal.

Fig. 13(a–c) demonstrates the time-domain Poynting vector (P) distributions of the memory cell in its low state, during triggering, and in its high state. This figure illustrates how the energy flux density changes as the memory cell transitions between these states, providing a clear visualization of the dynamic behavior of the device.

The performance of all-optical photonic crystal memory devices is highly dependent on input power levels, particularly regarding switching dynamics and contrast ratio. In the proposed structure, a continuous-wave input signal with power varying between 2.4 and 3 μW/μm was applied to Port A, followed by a trigger pulse similar to previous configurations. The experimental and simulation results are presented in Fig. 14, illustrating key trade-offs in system performance.Fig. 14a examines the relationship between input power and rise time, showing that as the input power increases, the rise time for the SET operation decreases from 0.7 ps to 0.2 ps, indicating improved switching speed. Meanwhile, Fig. 14b presents the effect of input power on contrast ratio, revealing a decline from 10 dB to 6 dB as power increases, a reduction attributed to enhanced nonlinear interactions that alter signal integrity. These observations highlight the inherent trade-offs in optimizing input power for performance stability in photonic crystal memory structures.

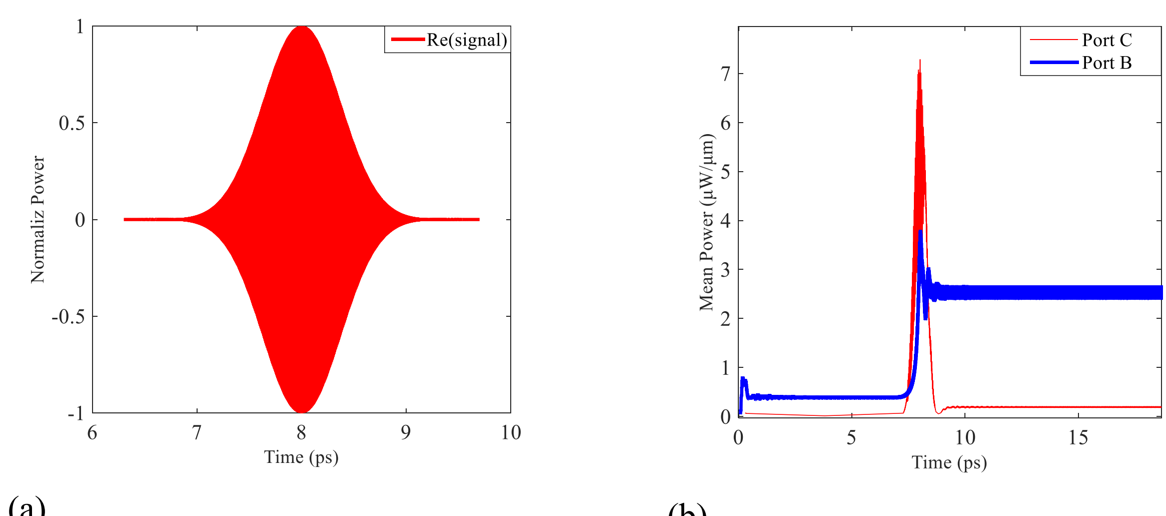

Fig. 12. Changing state of memory cell by applying a trigger signal over time: (a) Input normalized Gaussian signal applied to Port C. (b) Output at Port B and input at Port A signals over time.

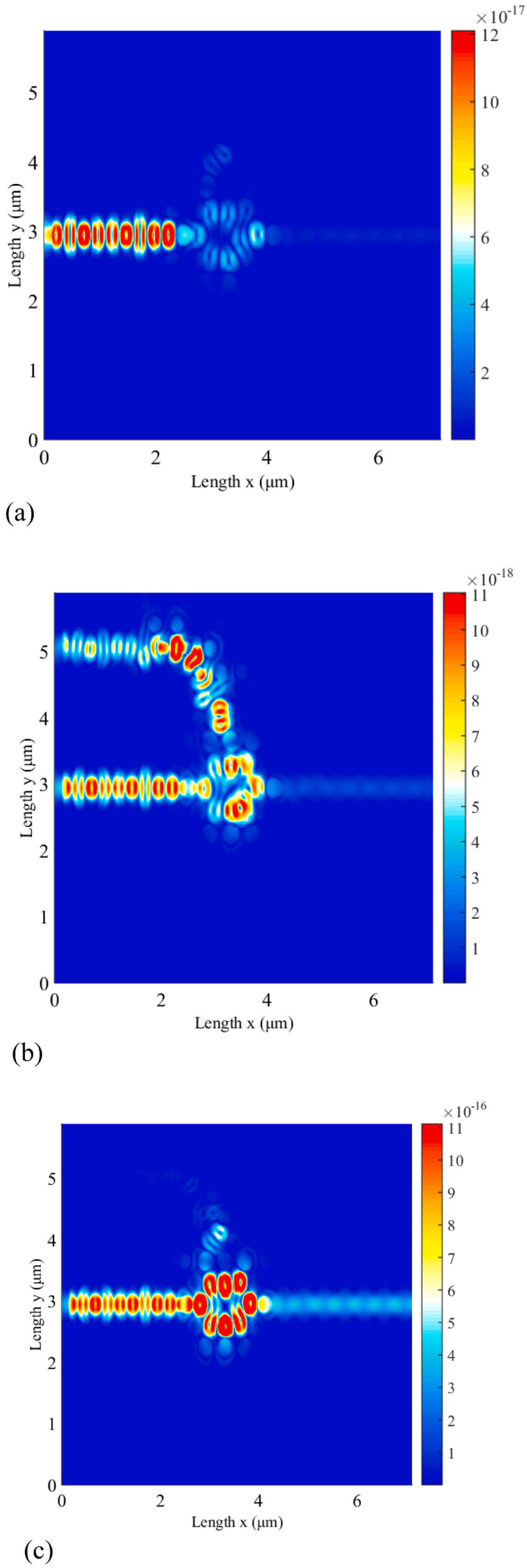

Fig. 13. Poynting vector (P) distributions of the proposed all-optical memory: (a) Low state. (b) Triggering time. (c) High state.

5. Tolerance analysis in fabrication

To evaluate the impact of fabrication tolerances, we conducted simulations considering variations of ±4 % in the air rod radii. As depicted in Fig. 15, a 4 % deviation in air rod size results in a 30 nm shift in the transmission resonance of the structure. This shift highlights the sensitivity of the design to minor fabrication errors, which can influence operational wavelength alignment.

However, in practical fabrication processes, the achievable precision is typically significantly better than the simulated worst-case scenario, ensuring that such errors remain minimal. In cases where minor fabrication imperfections do occur, the input wavelength can be adjusted within the resonance window of the structure to maintain optimal operation. This adaptive approach allows the device to function reliably even with small variations in structural parameters.

This analysis confirms the robustness of the design against fabrication uncertainties, ensuring consistent performance under realistic manufacturing conditions.

One of the critical parameters influencing the performance of photonic crystal-based structures is optical coupling efficiency. In hexagonal photonic crystal designs on a GaAs substrate, coupling efficiency is determined by several factors including fabrication precision, mode matching, and waveguide alignment. Typically, for wavelengths around 1550 nm, the coupling loss in air-clad photonic crystal systems falls within the range of 1.36 to 2.7 dB [43,44], depending on structural optimization. Through design refinements—such as optimizing the geometry, defect positioning, and excitation conditions—these losses can be minimized, thereby enhancing overall device performance.

In addition to coupling efficiency, temperature variations are another crucial factor affecting device performance through their influence on the material's nonlinearity. Based on experimental reports from various studies, an increase of 10 °C around room temperature (∼300 K) typically leads to an approximate 5–6 % decrease in the Kerr nonlinear coefficient (n_2) [37]. These thermal variations can significantly modulate the effective refractive index of the material, thus impacting the resonant behavior of the photonic device. To mitigate such temperature-induced effects, active temperature stabilization methods—such as thermoelectric cooling—or dynamic input wavelength tuning can be employed to compensate for resonance shifts and ensure that the device maintains its optimal performance over a wide range of operating temperatures.

Table 2 provides a comparison between this work and those reported in the literature. As seen, this work demonstrates a significant advancement in photonic crystal design, achieving a compact footprint of only 30 μm² for a hexagonal photonic crystal with air holes in GaAs operating at 1550 nm. This represents a substantial reduction in size compared to previous designs [40–44,37], improving integration density for future photonic integrated circuits. Furthermore, the response time of 0.21 psec surpasses many existing structures [40–43,37], highlighting the potential for high-speed applications. While the contrast ratio (6.98 dB) is competitive with the literature, further optimization may be explored to enhance this parameter. The utilization of established GaAs fabrication techniques suggests excellent manufacturability and scalability. This work therefore presents a compelling combination of miniaturization, speed, and practicality in photonic crystal technology.

6. Conclusion

In this paper, a new structure for an all-optical memory cell was proposed. A hexagonal photonic crystal with air rods on GaAs was used as the main platform for this structure. By utilizing FDTD simulations due to the nonlinear Kerr material properties in the photonic crystal cavity, we achieved high-speed performance with a rise time of <0.21 picosecond for state switching. The high confinement of light inside the hexagonal cavity and the use of Kerr material in this structure result in

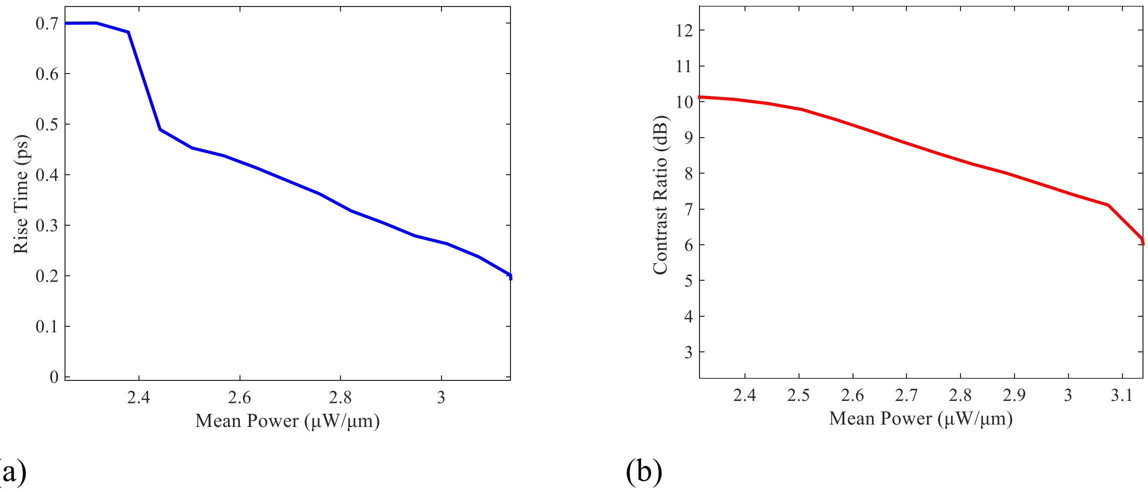

Fig. 14. Influence of input power on memory cell performance: (a) The effect of increasing input power on rise time, showing a reduction from 0.7 ps to 0.2 ps (b) The impact of input power on contrast ratio, illustrating a decrease from 10 dB to 6 dB.

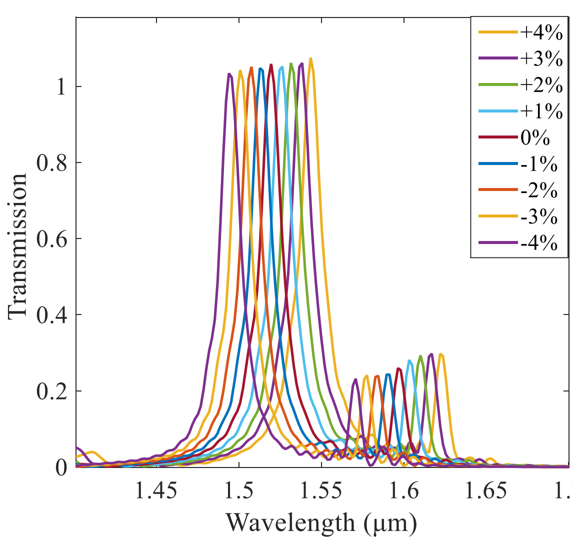

Fig. 15. Analysis of the impact of ±4 % fabrication error on the transmitted field intensity across wavelengths ranging from 1.4 to 1.7 μm.

low power consumption, with both signal and bias power being <3 μW/μm. Additionally, the reduction in the dimensions of the structure to approximately 30 μm^2 is notable compared to recent works. Furthermore, one of the notable features of the proposed structure is its operation at the telecommunication wavelength of 1.550 μm. The Contrast Ratio (dB) for this structure was calculated to be 6.98, and it can be increased by adjusting the design parameters of the proposed structure. Additionally, a comparison table between the proposed structure and recently presented structures is provided. As shown in the table, the proposed structure has significantly improved in terms of dimensions and speed. Beyond functioning as a single-unit memory cell, the proposed structure provides a foundation for designing various memory types, such as D, SR, and T-type memories. Due to its compact dimensions and low power consumption, this structure can be scaled for integration into larger memory arrays. By adjusting its design parameters for different wavelengths, multiple memory units can be configured accordingly. Furthermore, utilizing a wavelength division multiplexer allows for independent optical power distribution across multiple memory cells, enabling the simultaneous storage of multiple optical wavelengths without interference.

CRediT authorship contribution statement

Dariush Jafari: Writing – original draft, Software, Formal analysis, Conceptualization. **Mohammad Danaie:** Writing – review & editing, Validation, Supervision, Formal analysis, Conceptualization.

Declaration of competing interest

The authors declare that they have no known competing financial interests or personal relationships that could have appeared to influence the work reported in this paper.

Table 2
Comparisom between the obtained results and the results reported in the literature.

Ref	Type of Structure	Mechanisms and Effects	Operating Wavelength (nm)	Footprint (μm^2)	Response Time (psec)	Contrast Ratio (dB)	Year
[45]	Linear hexagonal lattice Si rods in air	Ring resonators and Y-splitters	1550	784	1.2	8.7	2022
[46]	Air holes in GaAs PhC configuration	MMI, scattering rods	1650	78.75	0.27	8.65	2021
[47]	Non-linear square lattice dielectric rods in air	cross-connected resonant cavities	1586 and 1620	361	3.1	9.68	2021
[48]	hexagonal photonic crystal	nonlinear Kerr effect	1550	28×28	1.6	8.7	2020
[49]	photonic crystal square air holes	Kerr effect and slow light phenomenon	1550 and 1604	15×15	1.35	–	2022
[50]	Si rods in SiO2	Ring resonator, OR and NOT logic gates, and T-splitter	1550	252	0.66	4.77	2024
This work	hexagonal photonic crystal Air holes in GaAs	Ring resonators	1550	30	0.21	6.98	2025

Data availability

Data will be made available on request.

References

[1] R.S. Tucker, The role of optics and electronics in high-capacity routers, J. Lightw. Technol. 24 (12) (2006) 4655–4673.

[2] H.J. Dorren, N. Calabretta, O. Raz, Scaling all-optical packet routers: how much buffering is required? J. Optic. Netw. 7 (11) (2008) 936–946.

[3] T. Nurmohammadi, K. Abbasian, R. Yadipoor, M.J As' adi, A novel proposal for OR/NOR logic gates based on dipole-induced transparency, Optik (Stuttg) 127 (18) (2016) 7115–7120.

[4] B. Li, M.I. Memon, G. Mezosi, Z. Wang, M. Sorel, S. Yu, Characterization of all-optical regeneration potentials of a bistable semiconductor ring laser, J. Lightw. Technol. 27 (19) (2009) 4233–4240.

[5] T. Nurmohammadi, K. Abbasian, M.J. As'Adi, D. Jafari, Design of an ultrafast all-optical NOR logic gate based on Mach-Zehnder interferometer using quantum-dot SOA, Optik (Stuttg) 125 (15) (2014) 4023–4029.

[6] N. Pleros, D. Apostolopoulos, D. Petrantonakis, C. Stamatiadis, H. Avramopoulos, Optical static RAM cell, IEEE Photon. Technol. Lett. 21 (2) (2008) 73–75.

[7] G. Mohammadi, A.A. Orouji, M. Danaie, A high-performance and high-resolution optical refractive index sensor using a compact photonic crystal ring resonator, Sens. Imaging 25 (1) (2024) 26.

[8] L. Hajshahvaladi, H. Kaatuzian, M. Danaie, Photonic crystal assisted excitation of surface plasmons: a high-resolution refractive index sensor based on a gold spiral in a photonic crystal resonator, Optic. Quant. Electron. 56 (9) (2024) 1417.

[9] L. Hajshahvaladi, H. Kaatuzian, M. Danaie, A very high-resolution refractive index sensor based on hybrid topology of photonic crystal cavity and plasmonic nested split-ring resonator, Photon. Nanostruct.-Fundam. Appl. 51 (2022) 101042.

[10] A.H. Nohoji, M. Danaie, Highly sensitive refractive index sensor based on photonic crystal ring resonators nested in a Mach–Zehnder interferometer, Optic. Quant. Electron. 54 (9) (2022) 574.

[11] L. Hajshahvaladi, H. Kaatuzian, M. Danaie, Design of a hybrid photonic-plasmonic crystal refractive index sensor for highly sensitive and high-resolution sensing applications, Phys. Lett. A 420 (2021) 127754.

[12] M. Danaie, B. Kiani, Design of a label-free photonic crystal refractive index sensor for biomedical applications, Photon. Nanostruct,-Fundam, Appl. 31 (2018) 89–98.

[13] L. Hajshahvaladi, H. Kaatuzian, M. Moghaddasi, M. Danaie, Hybridization of surface plasmons and photonic crystal resonators for high-sensitivity and high-resolution sensing applications, Sci. Rep. 12 (1) (2022) 21292.

[14] S. Noda, A. Chutinan, M. Imada, Trapping and emission of photons by a single defect in a photonic bandgap structure, nature 407 (6804) (2000) 608–610.

[15] M. Danaie, A. Geravand, S. Mohammadi, Photonic crystal double-coupled cavity waveguides and their application in design of slow-light delay lines, Photon. Nanostruct.-Fundam. Appl. 28 (2018) 61–69.

[16] L. Hajshahvaladi, H. Kaatuzian, M. Danaie, A.A. Nohiji, The effect of metal rods in a hybrid plasmonic-photonic crystal cavity design, in: In 2022 30th International Conference on Electrical Engineering (ICEE), IEEE, 2022, pp. 936–940.

[17] Z. Qiang, W. Zhou, R.A. Soref, Optical add-drop filters based on photonic crystal ring resonators, Opt. Express 15 (4) (2007) 1823–1831.

[18] E. Beiranvand, M. Danaie, M. Afsahi, A hybrid mode splitter for separation and excitation of photonic crystal odd and even modes using plasmonic waveguides, Photon. Nanostruct.-Fundam. Appl. 62 (2024) 101323.

[19] M. Danaie, H. Kaatuzian, Bandwidth improvement for a photonic crystal optical Y-splitter, J. Opt. Soc. Korea. 15 (3) (2011) 283–288.

[20] M. Danaie, R. Nasiri Far, A. Dideban, Design of a high-bandwidth Y-shaped photonic crystal power splitter for TE modes, Int. J. Opt. Photon. 12 (1) (2018) 33–42.

[21] A.H. Nohoji, P. Keshavarzi, M. Danaie, A photonic crystal waveguide intersection using phase change material for optical neuromorphic synapses, Opt. Mater. 151 (2024) 115372.

[22] E. Danaee, A. Geravand, M. Danaie, Wide-band low cross-talk photonic crystal waveguide intersections using self-collimation phenomenon, Opt. Commun. 431 (2019) 216–228.

[23] S.A. Khatami, P. Rezaei, M. Danaie, A.H. Daroonkola, Photonic crystal 180 ring-shaped hybrid: from microwave to optics, IEEE Photon. Technol. Lett. 33 (21) (2021) 1165–1168.

[24] D. Jafari, T. Nurmohammadi, M.J. Asadi, K. Abbasian, All-optical analog-to-digital converter based on Kerr effect in photonic crystal, Opt. Laser Technol. 101 (2018) 138–143.

[25] M.W. McCutcheon, G.W. Rieger, J.F. Young, D. Dalacu, P.J. Poole, R.L. Williams, All-optical conditional logic with a nonlinear photonic crystal nanocavity, Appl. Phys. Lett. 95 (22) (2009) 221102.

[26] C.J. Wu, C.P. Liu, Z. Ouyang, Compact and low-power optical logic NOT gate based on photonic crystal waveguides without optical amplifiers and nonlinear materials, Appl. Opt. 51 (5) (2012) 680–685.

[27] M. Moradi, M. Danaie, A.A. Orouji, Design of all-optical AND gate based on a hybrid photonic crystal and plasmonic structure, Optic. Quant. Electron. 56 (4) (2024) 577.

[28] A. Farmani, R. Beyranvand, Numerical modeling of a compact and high contrast reversible all optical feynman gate with nonlinear kerr effects based on two dimensional photonic crystals, Appl. Electromagnet. 9 (2) (2021) 9–15.

[29] K. Asakawa, Y. Sugimoto, Y. Watanabe, N. Ozaki, A. Mizutani, Y. Takata, Y. Kitagawa, H. Ishikawa, N. Ikeda, K. Awazu, X. Wang, Photonic crystal and quantum dot technologies for all-optical switch and logic device, New J. Phys. 8 (9) (2006) 208.

[30] S. Khani, M. Danaie, P. Rezaei, Hybrid all-optical infrared metal-insulator-metal plasmonic switch incorporating photonic crystal bandgap structures, Photon. Nanostruct.-Fundam. Appl. 40 (2020) 100802.

[31] A. Shinya, S. Mitsugi, T. Tanabe, M. Notomi, I. Yokohama, H. Takara, S. Kawanishi, All-optical flip-flop circuit composed of coupled two-port resonant tunneling filter in two-dimensional photonic crystal slab, Opt Expr. 14 (3) (2006) 1230–1235.

[32] E. Beiranvand, M. Danaie, M. Afsahi, An efficient coupling scheme between photonic crystal waveguides and plasmonic metal-insulator-metal waveguides, Plasmonics 20 (2) (2025) 701–708.

[33] E. Beiranvand, M. Danaie, M. Afsahi, Design of photonic crystal horn antenna for transverse electric modes, Optic. Applicata 50 (3) (2020) 401–413.

[34] A. Geravand, M. Danaie, S. Mohammadi, All-optical photonic crystal memory cells based on cavities with a dual-argument hysteresis feature, Opt. Commun. 430 (2019) 323–335.

[35] D. Fitsios, T. Alexoudi, A. Bazin, P. Monnier, R. Raj, A. Miliou, G.T. Kanellos, N. Pleros, F. Raineri, Ultra-compact III−V-on-Si photonic crystal memory for flip-flop operation at 5 gb/s, Opt. Express 24 (4) (2016) 4270–4277.

[36] M. Merklein, B. Stiller, K. Vu, S.J. Madden, B.J. Eggleton, A chip-integrated coherent photonic-phononic memory, Nat. Commun. 8 (1) (2017) 1–7.

[37] L. Liu, R. Kumar, K. Huybrechts, T. Spuesens, G. Roelkens, E.J. Geluk, T. De Vries, P. Regreny, D. Van Thourhout, R. Baets, G. Morthier, An ultra-small, low-power, all-optical flip-flop memory on a silicon chip, Nat. Photon. 4 (3) (2010) 182–187.

[38] E. Kuramochi, K. Nozaki, A. Shinya, K. Takeda, T. Sato, S. Matsuo, H. Taniyama, H. Sumikura, M. Notomi, Large-scale integration of wavelength-addressable all-optical memories on a photonic crystal chip, Nat. Photon. 8 (6) (2014) 474.

[39] M. Notomi, T. Tanabe, A. Shinya, E. Kuramochi, H. Taniyama, S. Mitsugi, M. Morita, Nonlinear and adiabatic control of high-Q photonic crystal nanocavities, Opt Express 15 (26) (2007) 17458–17481.

[40] W. Bogaerts, S.K. Selvaraja, Compact single-mode silicon hybrid rib/strip waveguide with adiabatic bends, IEEE Photon. J. 3 (3) (2011) 422–432.

[41] S.K. Selvaraja, W. Bogaerts, D. Van Thourhout, Loss reduction in silicon nanophotonic waveguide micro-bends through etch profile improvement, Opt. Commun. 284 (8) (2011) 2141–2144.

[42] R.W. Boyd, A.L. Gaeta, E. Giese, Nonlinear optics. Springer Handbook of Atomic, Molecular, and Optical Physics, Springer International Publishing, Cham, 2008, pp. 1097–1110.

[43] H. Nakamura, Y. Sugimoto, K. Kanamoto, N. Ikeda, Y. Tanaka, Y. Nakamura, S. Ohkouchi, Y. Watanabe, K. Inoue, H. Ishikawa, K. Asakawa, Ultra-fast photonic crystal/quantum dot all-optical switch for future photonic networks, Opt. Express 12 (26) (2004) 6606–6614.

[44] I. Fushman, D. Englund, A. Faraon, N. Stoltz, P. Petroff, J. Vuckovic, Controlled phase shifts with a single quantum dot, Science 320 (5877) (2008) 769–772.

[45] S. Soma, M.V. Sonth, S.C. Gowre, Design of two-dimensional photonic crystal based ultra compact optical RS flip-flop, Photon. Netw. Commun. 43 (2022) 109–115.

[46] K.M.K. Rao, N.J. Aneela, K.Y. Sri, K.N. Prasanna, N. Sahithi, L. Likhitha, Design of clocked Jk flip flop using air hole structured photonic crystal, J. VLSI Circuit. Syst. 3 (2021) 11–20.

[47] S.S. Zamanian-Dehkordi, M. Soroosh, G. Akbarizadeh, An ultra-fast all-optical RS flip-flop based on nonlinear photonic crystal structures, Opt. Rev. 25 (2018) 523–531.

[48] S. Soma, M.V. Sonth, S.C. Gowre, Design of two-dimensional photonic crystal based ultra compact optical RS flip-flop, Photon. Netw. Commun. 43 (2) (2022) 109–115.

[49] S. Mirzaiee, M. Noori, H. Baghban, H. Veladi, All-optical memory based on slow light and Kerr effect in photonic crystal platform with independent write/read/hold control, Physic. Scripta 97 (6) (2022) 065502.

[50] F. Parandin, P. Karami, Numerical analysis of All-Optical universal NAND and NOR photonic crystal logic gates by creating holes in silicon material, Opt. Laser Technol. 182 (2025) 112197.

Dariush Jafari is currently pursuing his PhD in Electrical Engineering at Semnan University, where his research focuses on the design and analysis of advanced optical components utilizing photonic crystal and plasmonic platforms. He has published five peer-reviewed papers in reputable journals, showcasing innovative contributions to the field of optical device engineering. His work emphasizes the development of high-performance and compact photonic structures, with applications in photonic integrated circuits and optical communication systems.

Mohammad Danaie received his BSc and MSc degrees from Ferdowsi university of Mashhad in 2005 and 2007 respectively with honors and his PhD degree from Amirkabir University of Technology in 2011. He has been an assistant professor of electrical engineering at Semnan University, Semnan, Iran since 2012, an associate professor since 2018 and a professor since 2024. He is the author and co-author of >100 peer reviewed journal papers and dozens of conference papers. His current research interests include nanophotonic devices, plasmonics, Integrated optics, photonic crystals, optical memories and graphene.